Evolution of a confined turbulent jet in a long cylindrical cavity: Homogeneous fluids

S. I. Voropayev,[1,2,a)] X. Sanchez,[1,3] C. Nath,[1] S. Webb,[4] and H. J. S. Fernando[1,5]
[1]*Environmental Fluid Dynamics Laboratories, Department of Civil Engineering and Geological Sciences, University of Notre Dame, Notre Dame, Indiana 46556, USA*
[2]*P.P. Shirshov Institute of Oceanology, Russian Academy of Sciences, Moscow 117851, Russia*
[3]*Physics Department, University of Girona, Girona 17071, Catalonia, Spain*
[4]*Geotechnology and Engineering Department, Sandia National Laboratories, P.O. Box 5800 MS-0706, Albuquerque, New Mexico 87185-0706, USA*
[5]*Department of Aerospace and Mechanical Engineering, University of Notre Dame, Notre Dame, Indiana 46556, USA*

(Received 28 April 2011; accepted 18 October 2011; published online 29 November 2011)

The flow induced in a long cylinder by an axially discharging round turbulent jet was investigated experimentally with applications to crude oil storage in the U.S. strategic petroleum reserves (SPR). It was found that the flow does not reach a true steady state, but vacillates periodically. Digital video recordings and particle image velocimetry were used to map the flow structures and velocity/vorticity fields, from which the frequency of jet switching, jet stopping distance, mean flow, turbulence characteristics, and the influence of end-wall boundary conditions were inferred. The results were parameterized using the characteristic length D and velocity $J^{1/2}/D$ scales based on the jet kinematic momentum flux J and cylinder width D. The scaling laws so developed could be used to extrapolate laboratory observations to SPR flows. © *2011 American Institute of Physics*. [doi:10.1063/1.3662442]

I. INTRODUCTION

The U.S. strategic petroleum reserves (SPR) consists of a collection of approximately cylindrical caverns, artificially created by leaching underground salt deposits. Operated by the U.S. Department of Energy, SPR are primarily located in the southern coasts of LA and TX. The caverns are roughly 700 m high and 70 m in diameter, with their roof at a depth of about 700 m (Ref. 1). Crude oil stored in these low aspect ratio (width/height ~0.1) caverns is periodically removed from the bottom, degassed and re-introduced near the top as a jet to maintain the oil quality. The jet nozzle diameter is much smaller than the cavern diameter. The depth of mixing and the velocity distribution of such jets influence the efficiency of oil refilling, and for no mixing the efficiency is maximum. The cavern flow falls into the category of confined jet flows. Some of their features include the limited depth x^* of jet penetration, rapid decrease of vertical velocity and a recirculating region between the jet and confining walls.

At high Reynolds numbers, confined jets often exhibit low frequency instability, oscillating behavior, large coherent structures and recirculating cells even when the flow boundary conditions are held symmetric and steady. The oscillatory phenomenon has been identified in numerous studies via direct velocity/pressure measurements, visualization and numerical simulations.[2–4] These oscillations lead to strong mixing in the upper part of caverns, and hence their characteristics are of importance for improving SPR performance and decreasing the cost of cavern degassing operations.

Although jet oscillations in long two-dimensional cavities have been documented for some 50 years,[5] with more recent work delving into basic flow structures and characteristics of turbulence,[2,6–10] no reliable parameterizations exist that can be used to extrapolate laboratory results to large cylindrical caverns. Confined round jets have also been used in a number of previous experiments.[11,12] In these studies, however, the main interest has been to obtain flow characteristics at distances larger than the jet penetrating distance $x > x^*$, in the region of weak turbulence.[7] No general parameterizations are available for typical mean velocity at $x \leq x^*$.

In this paper, the evolution of a round turbulent jet released into a low-aspect-ratio cylindrical container filled with a homogeneous fluid is investigated experimentally. The goal was to model the degas flow configuration in SPR caverns (closed top and bottom) with the purposes of clarifying the general flow structure, mechanism of jet stopping and the role of end conditions while developing parameterizations for the frequency of flow oscillations and mean and turbulent flow velocities as a function of external parameters.

Digital video recordings and particle image velocimetry (PIV) were used to delineate and quantify flow structures and obtain flow parameters of consequence (velocity/vorticity, frequency of oscillations). This is a step toward understanding confined jet flows in the presence of such additional complexities as background stratification and side wall heating due to geothermal heat flux, as in the case of SPR caverns.

II. EXPERIMENTAL SET-UP AND METHOD

In most of the experiments, the flow was generated in a circular glass cylinder of length $L = 65$ cm, inner diameter

a)Author to whom correspondence should be addressed. Electronic mail: s.voropayev@nd.edu. Tel.: (574) 631-3467.

$D = 10$ cm ($L \gg D$) and thickness 0.5 cm, with closed top and bottom. In some runs, a smaller cylinder ($D = 4.5$ cm, $L = 45$ cm) was also used. To minimize optical distortions due to curvature, the cylinder was placed in a larger ($75 \times 75 \times 25$ cm^3) square Plexiglas tank filled with distilled water; see the schematic in Fig. 1. This tank (1) was painted black, and the water level (2) was above the top surface of the cylinder (3). In most of the experiments, the "bottom" end of the cylinder was sealed by a glass disk, while the "top" end was closed by a glass disk (4) with a small circular hole (diameter 1.5 cm) at the centre. The jet flow (5) inside the cylinder was generated using a conical round nozzle (6) placed at the centre of the hole in the top disk (4). The inner nozzle diameter was $d = 0.165$ cm while the outer diameter was 0.5 cm, which is less than the diameter of the hole in the glass disk (4). A precision calibrated pump (7) takes water from the larger tank and feeds the nozzle (6) with relatively small volume flux q, generating an intense turbulent jet with a substantial momentum flux J. The same amount of fluid, but with negligible momentum, leaves the cylinder through the hole in the top cover (4). Although most of the measurements were conducted with both ends closed, to better understand the mechanism of jet break up, additional experiments were conducted with different (top/bottom) boundary conditions.

The dimensional Cartesian coordinate (x, y, z) system used and associated dimensional velocity components (u, v, w) are shown in Fig. 1. The instantaneous velocity component is presented as a sum of the mean and fluctuating parts, i.e., $u = \overline{u} + u'$. A similar notation is used for dimensionless velocity, i.e., $U = \overline{U} + U'$. The velocity data were obtained mostly in the (x-y) plane along the cylinder axis using particle image velocimetry (PIV). In selected runs, to clarify the mechanism of jet oscillations, additional data on cross-flow velocity components were obtained in the (y-z) plane by interchanging the positions of camera and laser.

To this end, the water in the cylinder was seeded with highly reflective Pliolite tracer particles (diameter $d_0 = 100\ \mu$m) having a small response time ($d_0^2/18\nu < 0.0005$ s; see Ref. 13), thus ensuring that particles follow fluid motion. A commercial PIV system (TSI Incorporated) was used, which includes: a Dual Nd:YAG Laser (8) (output 90 mJ/pulse, pulse duration 6 ns) with optics to produce a thin ($\Delta h \approx 0.3$ cm) horizontal light sheet (9) that spreads along the cylinder axis through a transparent gap (10), a Laser-Pulse Synchronizer and a CCD camera (11) (PIVCAM 10-30, 1024×1024 pixels). The camera, laser and the synchronizer were connected to a control computer, and data processing was conducted using the TSI PIV software package Insight^{TM}. Pairs of images were captured at a fixed frequency (15 Hz with 2.5 ms time shift in between) over the duration of the experiment (typically 30 s), and transferred to the computer. The duration was restricted by the number of image pairs ($\sim$450) that could be stored on the computer RAM. The data were later transferred to the hard drive, where the horizontal velocity and vertical vorticity fields were calculated from each pair of frames using Insight^{TM}.

The PIV images in (x-y) plane had a space resolution of about 0.075 cm/pixel. The area of observations was 65×10 cm^2 with an interrogation area of 32×32 pixels, and the data were interpolated onto a grid (4×4 pixels). Numerous commercial (TSI) algorithms are available to calculate velocity fields from image pairs, but the standard Nyquist algorithm (50% overlap) produced the best results with minimum number of erroneous vectors. Obvious spurious vectors ($<$1-2%) were removed and substituted by "averaged" interpolated values. No additional averaging or smoothing was used. Information was stored as vector files, on a 204×34 matrix ($\sim$0.3 cm spatial resolution) that contain digitized values of horizontal velocity components for each image pair ($\sim$450 vector files for each run). The resulting vector files were used in two ways. First, using TECPLOT software, instantaneous and averaged velocity/vorticity fields were plotted (see examples below), and the analysis was done frame by frame or using TECPLOT animation option. After preliminary analyses, the data from vector files were processed using MATLAB.

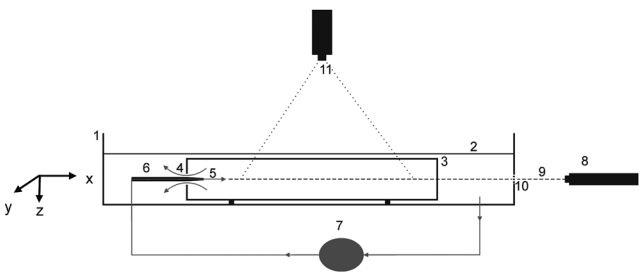

FIG. 1. Experimental set-up: 1—tank ($75 \times 75 \times 25$ cm^3) painted in black with water; 2—water level inside the tank; 3—glass cylinder (diameter $D = 10$ cm, length $L = 65$ cm) seeded with small Pliolite particles; 4—small hole for outflow; 5—inflow; 6—nozzle ($d = 0.165$ cm); 7—calibrated pump; 8—laser; 9—horizontal light sheet; 10—transparent gap; 11—CCD (for PIV) or DVC (for video) camera. Cartesian coordinates (x, y, z) are shown to the left, with origin at the centre of the nozzle. In most experiments, only the horizontal (u, v) velocity components were measured in (x-y) plane along the cylinder axis. In some runs additional data on across flow velocity components (v, w) were obtained in a vertical plane (y-z). In the latter experiments, the camera and laser were interchanged.

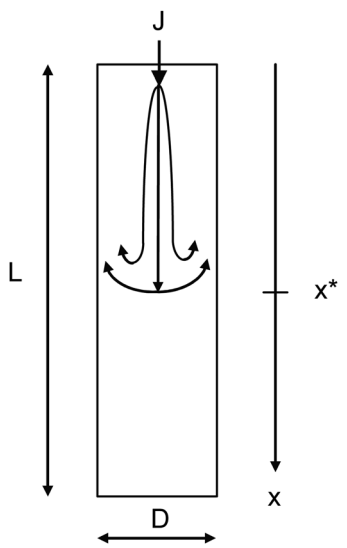

FIG. 2. A schematic of mean flow in a long cylinder and external parameters.

In addition to PIV, digital video recordings were used for visual observations and analysis. Here, the flow was seeded with larger Pliolite particles (diameter ~0.25 mm) but with a lower concentration than that used for PIV to prevent overlapping of particle "streaks." The camera used was DVC-3400 (DVC Company), and a 300 mJ continuous laser was used for illuminating the flow field. The camera was free-running (frequency 10 Hz) and particle streak images were obtained from these digital video recordings. This method was useful in mapping the global flow structure and for visually observing the period of flow oscillations. The recordings of duration 100-200 s were replayed at a slow speed (1-5 Hz) and analyzed manually; some characteristic images are given below (Fig. 5).

To better visualise the central part of the jet, in selected runs, smaller tracer particles were introduced continuously at the nozzle. The resulting images give the streamlines issued from the nozzle and are used below (Fig. 3) to illustrate the jet structure. The DVC resolution was not enough for smaller tracer particles, for which a still digital camera of high resolution was used.

The experiments with PIV measurements and DVC recordings covered five jet Reynolds numbers ($Re = 10\,100$, 12 700, 15 300, 17 900, 23 100; defined below). Each experiment was repeated five times to improve statistics. For averaging, the PIV data were processed by using 5 data segments (5×450 pairs of frames) for each run. To obtain more data on the frequency of flow oscillations, six additional experiments ($Re = 2800$, 5900, 9100, 12 200, 18 400, 24 600) were conducted where long DVC records were made; no PIV measurements were made in these runs.

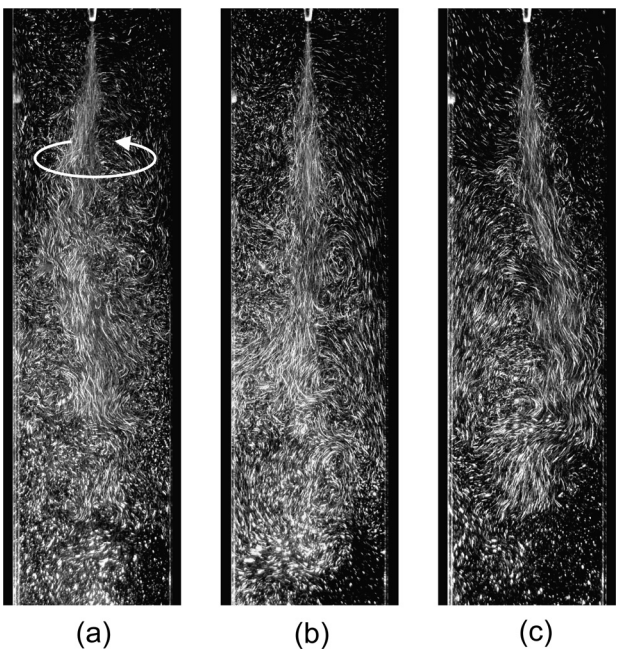

FIG. 3. Particle streak images showing the central part of the jet at different times. In (a)—jet is tilted to the left and slowly rotates azimuthally (white arrow) around the cylinder axis, in (b)—jet continues its azimuthal rotation and becomes visible near the cylinder centreline, in (c)—it becomes tilted to the right. The direction of rotation changes periodically with time. In this experiment $Re = 10\,100$ and an exposure of 0.05 s was used. To visualise the streamlines, smaller tracer particles were introduced directly into the nozzle.

Although in most of experiments the cylinder was positioned horizontally (Fig. 1), for convenience, it is shown vertically in the following illustrations.

III. GENERAL FLOW BEHAVIOUR AND SCALING ANALYSIS

A. General flow behaviour

Upon initiation, the jet propagates relatively quickly along the cylinder with a characteristic spherical front. Nevertheless, in contrast to unconfined jets, where the front propagates over large distances, the jet front in a low-aspect-ratio cylinder suddenly stops at some critical distance x^* from the origin (see schematic in Fig. 2), loses its coherence and breaks down into smaller eddies forming, at $x \sim x^*$, the so-called weak "diffusive turbulence."[7] Thereafter, fluid motions decay rapidly with distance and at $x > x^*$ the fluid visually appears still.

In the upper part of the cylinder, $x < x^*$, however, the motion remains energetic and large "coherent" eddies are frequently visible in the flow surrounding the central part of the jet. Visually the flow never reaches a strict steady state but changes periodically with a characteristic frequency f in rather complex manner.

To understand the general flow structure, extensive observations of DVC recordings and PIV measurements were made in both along flow (x-y) and across flow (y-z) planes, and the results are summarized below.

Schematically, the established flow can be depicted as (i) primary jet flow with relatively high velocity and (ii) secondary recirculation cell(s) with smaller velocities. Typical particle streak images showing mostly the central part of the

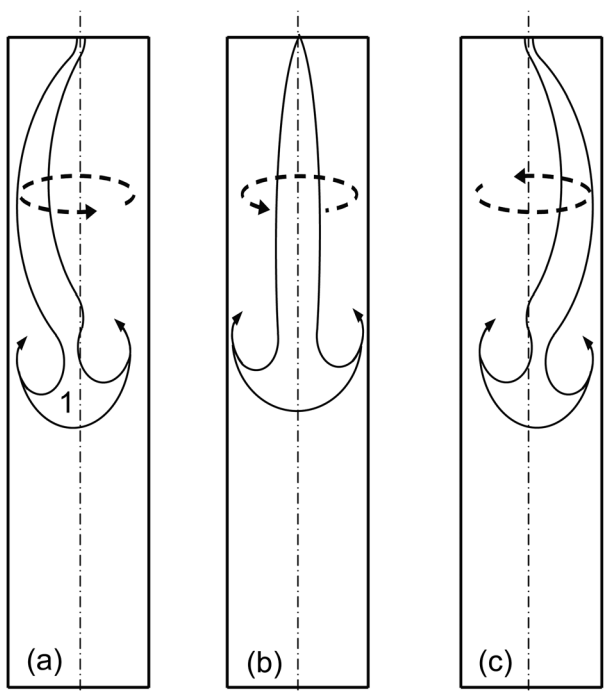

FIG. 4. A schematic of periodic flow precession (a-c) around cylinder axis as observed in the (x-y) plane during half of the period. Observations show that this instability originates in the jet frontal area (1) and propagates upstream. The direction of precession (arrow) changes periodically.

jet in the (*x*-*y*) plane at different times are shown in Fig. 3. At the first glance, the jet appears to be simply oscillating periodically in the (*x*-*y*) plane, similar to flipping oscillations of two-dimensional jets. More detailed observations in the (*x*-*y*) plane and additional observations in (*y*-*z*) (see below), however, show that the jet is spiraling periodically around the cylinder axis (precessing mode). Such (azimuthal) precession has been observed previously in studies of flame stability in swirling flows with rapid expansion and later in similar flows with large expansion ratio and no upstream swirl.[14]

In Fig. 3(a) the jet is visible as deflected to the left and slowly rotates azimuthally around the cylinder axis, in (b) the jet continues its azimuthal rotation and becomes visible near the cylinder centreline, and in (c) the jet is deflected to the right. A schematic of periodic flow precession around the cylinder axis in the (*x*-*y*) plane is given in Fig. 4.

The analysis of DVC recordings shows that the flow is dominated by large eddies that arise rather spontaneously, grow in size due to merger of smaller eddies and form large recirculation cells adjacent to side walls (Fig. 5). Observations in (*x*-*y*) plane show that cells reside for a while and then almost disappear only to recur (within the light sheet) in the opposite side after some time.

As shown schematically in Fig. 6(a), the secondary flow is approximately axisymmetric with jet in the central part, accompanied by a toroidal recirculation cell, which is visible

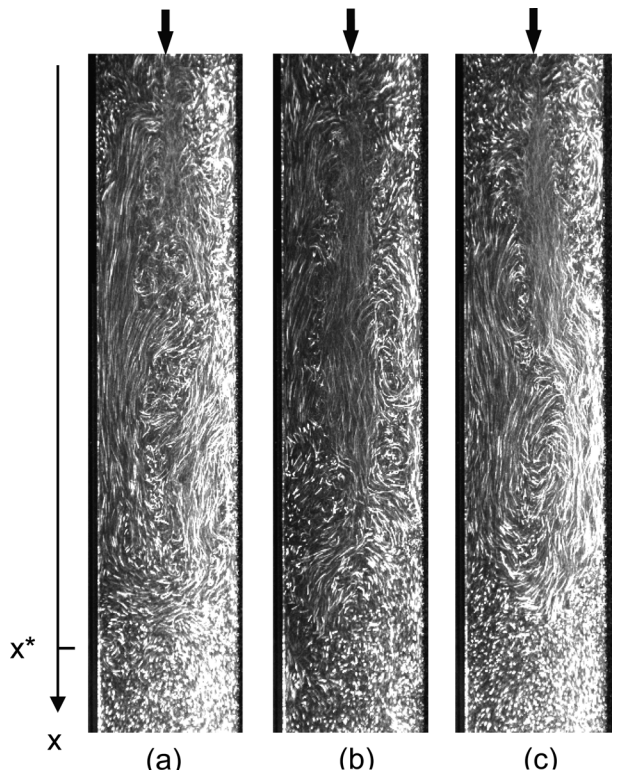

FIG. 5. Typical particle streak images, showing large coherent eddies and periodic flow oscillations in the (*x*-*y*) plane. The flow was seeded with relatively large tracer particles and the central part of the jet is not well visible. In (a)—large recirculation cell is visible along the right side of the image, in (b)—two approximately symmetric cells are visible along both sides, in (c)—large cell is visible along the left side. The nozzle is shown by black arrow, $Re = 10\,100$ and an exposure of 0.1 s was used.

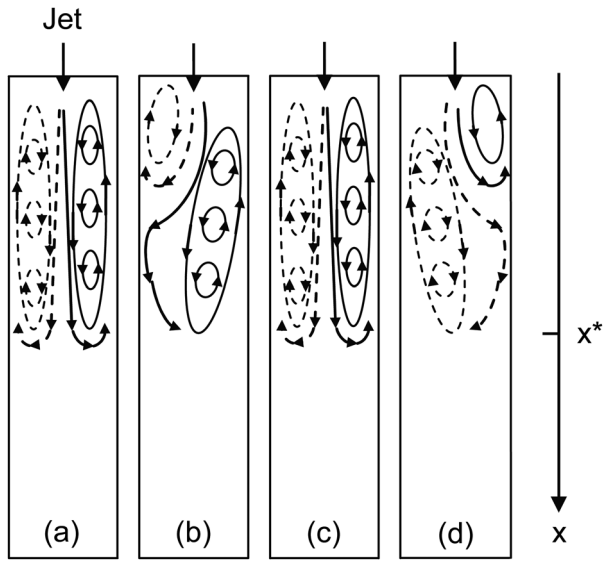

FIG. 6. A schematic of the evolution of flow structures during an oscillation period in the *x*-*y* plane. Dashed and solid lines show clockwise and anticlockwise motions, respectively. (a)—the flow approximately is axisymmetric with toroidal recirculation cell, which is visible as two symmetric elongated elliptic cells carrying smaller eddies; (b)—the flow breaks its symmetry, toroidal cell is deformed and becomes visible as two asymmetric cells; (c)—the flow passes through its symmetric state, forming in (d) a large intense cell at the left and small weaker cell at the right; symmetric state (a,c) sometime is not well visible and the flow vacillates between (b) and (d) by precessing along the cylinder axis (Fig. 4).

in the (*x*-*y*) plane as two symmetric elongated elliptical cells filled with smaller eddies. In (b) the flow loses its symmetry, central jet migrates to the left, toroidal cell is deformed and becomes visible in the (*x*-*y*) plane as two asymmetric cells—larger in the right and smaller in the left. In (c) the flow again passes through its approximately symmetric state, forming in (d) a large intense cell to the left and a small weaker cell to the right. Thereafter the process repeats itself. Symmetric state (a,c) is sometime unclear, and the flow vacillates between (b) and (d) by precessing along the cylinder axis as shown in Fig. 4.

The analysis of DVC recording and PIV images shows that at small distances $x < 0.5D$ only a narrow energetic central jet remains nominally steady (Fig. 3), while the near-wall recirculation cells are formed periodically in the outer flow at $0.5D < x < 3D$ (Fig. 5).

Figure 7 shows averaged PIV data of the transverse velocity magnitude in the across flow (*y*-*z*) plane for different distances from the origin. Axisymmetric diverging jet flow is visible near the cylinder axis at small and moderate distances (a,b). At larger distances (c) the jet is not evident and at $3D < x < 4D$ the flow can be described as a spherical frontal area of size D in chaotic motion (see Figs. 2 and 4). Visually the rotational flow instability originates in this frontal area, which periodically rotates slowly in one or another direction, initiating the deflection of upstream jet toward the wall followed by precession.

Typical streak images and PIV data for instantaneous across flow velocity (v, w) and axial vorticity are shown in Fig. 8. In Fig. 8(a), the fluid rotates mostly clockwise and the net angular momentum M in the along flow direction is

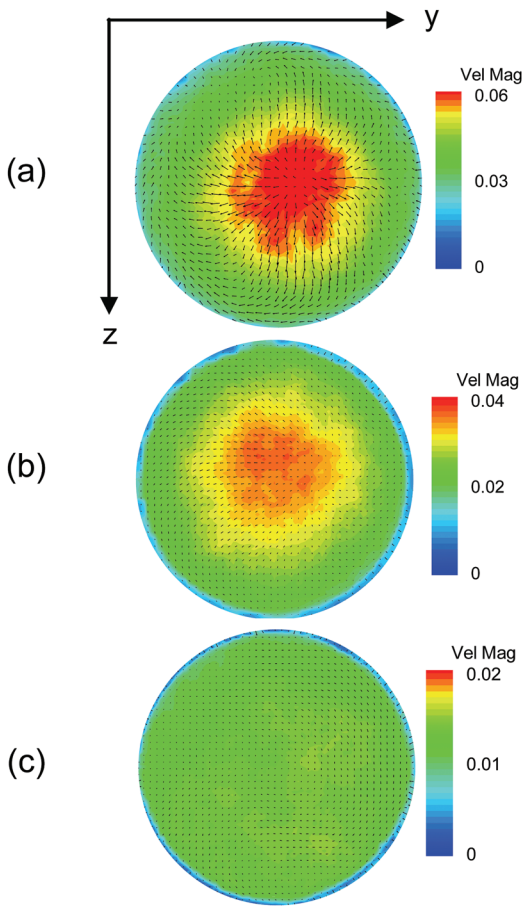

FIG. 7. (Color) Transverse velocity magnitude (averaged over ~100 periods; colour scale is in ms^{-1}) in (y-z) plane for different distances from the nozzle: $x/D = 1.5$ (a), 2.5 (b), 3.5 (c). Note that the scale is different for each image, and the rapid decrease of transverse velocity at the jet axis.

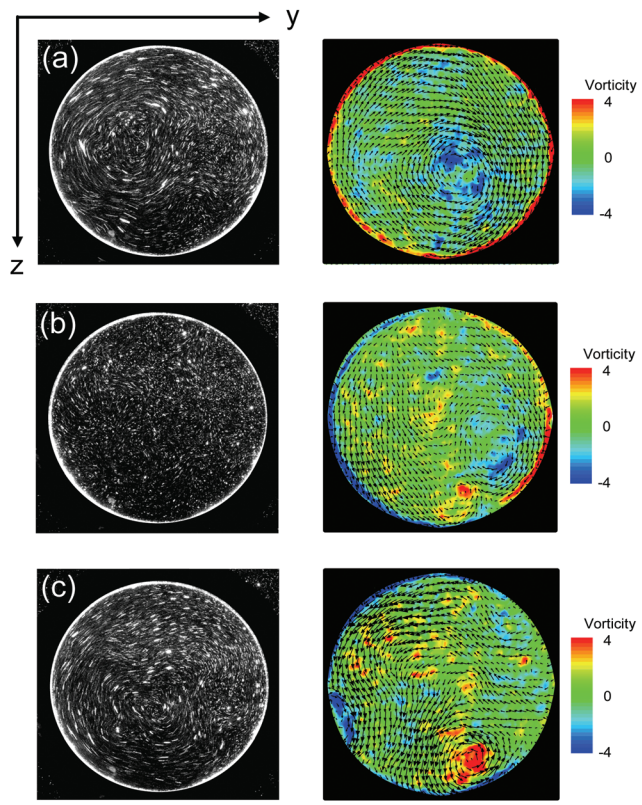

FIG. 8. (Color) Left column—particle streak images in the (y-z) plane; Right column—PIV data for vorticity (different colours) and velocity (black arrows) in a transverse plane. (a)—fluid rotates mostly clockwise and the net angular momentum M is negative; (b)—direction of rotation changes and the net angular momentum is near zero; (c)—fluid rotates mostly counter clockwise and the net angular momentum is positive. $Re = 10\,100$, $X = x/D = 3.5$. Thin near-wall boundary layers with sharp variation of azimuthal vorticity are seen in vorticity data.

negative. In Fig. 8(b), the direction of rotation changes and the net angular momentum is near zero. In Fig. 8(c) the net angular momentum is positive.

Using PIV data for across flow (y-z) velocity components (v, w), the (kinematic) angular momentum M (per unit length of the cylinder) was calculated as a function of time, t, as $M(t) = \iint_S [v(t)z - w(t)y]dydz$ (S—cylinder cross section), and the results are shown in Fig. 9. As can be seen, M changes periodically from positive to negative, indicating periodic switching between clockwise and counter clockwise rotation. A typical period of $1/f \sim 10$ s is evident from this record, and spectral analysis gives $f = 0.089$ Hz as the dominant frequency. This agrees well with the frequency of jet oscillations observed in the along flow (x-y) plane (see Fig. 16 below).

Although M switches between positive and negative values (Fig. 9), detailed observations show that the fluid as a whole has only little rotation relative to the cylinder axis. Instead, eddies of opposite sign of rotation (swirl) are observed. They interact with each other in complex manner, periodically forming one or two larger eddies with significant amount of swirl relative to the eddy axis. These larger eddies precess by spiraling periodically relative to the cylinder axis. For smaller distances the results were more "noisy" and the spectral peak was less sharp. Therein the axial jet velocity u is strong (see below) and PIV measurements of across flow (v, w) velocity are not accurate, since tracer particles crossing the light sheet are visible only for very short time.

The description above is based on observations in two planes, whilst the real flow is three-dimensional. Nevertheless, extensive observations show that the flow is clearly unstable with a dominant rotational instability (precession mode), and the global flow structure changes periodically with a characteristic frequency f.

The physical mechanism that impedes jet propagation in a long cylinder is discussed next, precursor to developing

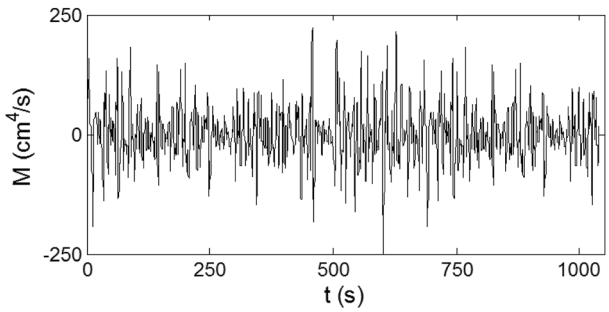

FIG. 9. Kinematic angular momentum M (per unit cylinder length) as a function of time t ($Re = 10\,100$, $X = x/D = 3.5$).

scaling and similarity analyses. The evaluation of scaling using PIV and DVC measurements will be given thereafter.

B. Boundary conditions and jet dissolution

The driving force for this flow configuration is the (kinematic) momentum flux J (force per unit mass) of the jet, which is related to the fluid velocity at nozzle exit (contributions from pressure and viscous stresses are negligible at the nozzle exit[15]). For a free jet, the net momentum flux is conserved along the flow, which allows the jet to propagate a large distance from the origin. In contrast, the jet flow in a closed low aspect ratio cylinder stops at $x > x^*$. Prima facie this can be construed as due to side-wall influence, where the viscous drag reduces the axial velocity. Observations show, however, that velocity near the wall is in the opposite direction due to recirculation cells (see Fig. 6 and Figs. 11(a) and 11(b) below), axial momentum decay cannot be accounted by the lateral viscous friction, and hence pressure gradients induced by end walls remain the only possible mechanism for jet stoppage. This contrasts the case of free jets, where outside pressure may be neglected.[16]

To clarify the role of end wall boundary conditions, additional experiments were conducted with the same jet intensity J but with different boundary conditions: both ends of the cylinder were closed but with provisions for the flow to exit through a coaxial opening surrounding the nozzle (Fig. 10(a)); the top of the cylinder open and the bottom closed (Fig. 10(b)); bottom open while the top closed (Fig. 10(c)); and both top and bottom open (Fig. 10(d)). Observations showed that flows in (a-c) were visually identical, in that the stoppage of the jet at $x \approx x^*$ was followed by periodic jet oscillations with approximately the same frequency and global flow structure. Quantitative PIV data confirm this conclusion. Figures 11(a) and 11(b) show that the mean vorticity and mean axial velocity distributions are practically the same for cases where either the top or the bottom is closed. The case with both ends closed is indistinguishable from these two cases (not shown). The case of both open ends (Fig. 10(d)), however, showed completely different behaviour (Fig. 11(c)). After the jet was initiated, the flow in the entire cylinder started moving, soon establishing a flow much like that through a pipe. Once the steady flow was established, the flow did not have visible oscillations.

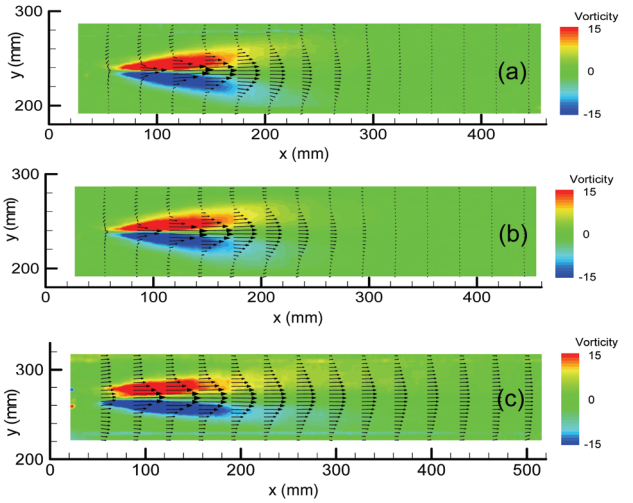

FIG. 11. (Color) PIV data of mean axial velocity (arrows) and mean vorticity (color coding, in s^{-1}) for three experiments at $Re = 10\,100$: (a) top open and bottom closed, (b) bottom open and top closed, (c) both top and bottom open. Ensemble averaging over 5×450 data frames was used. For clarity, only every eighth velocity profile is shown.

The above results can be explained by considering momentum flux transformation under different cylinder end conditions. When only the bottom of the cylinder is closed (e.g., Fig. 10(b)), the action of the momentum source J leads to an opposing pressure distribution in the cylinder (see Cantwell[17] for a related discussion) with a mean (over the cylinder cross section) pressure p distribution shown schematically in Fig. 10(b). If viscous losses near lateral boundaries are neglected, then the conservation of momentum determines the mean pressure p_0 at the bottom of the cylinder as

$$p_0 \approx \rho J / S, \tag{1}$$

where ρ is the fluid density and $S = \pi D^2/4$, so that the net force at the bottom is ρJ. The momentum flux J transforms to a pressure distribution that opposes the motion, acts on the bottom/top of the cylinder and leads to the jet stoppage at some distance x^*.

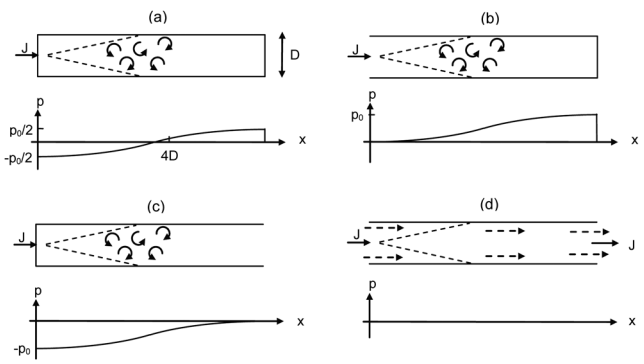

FIG. 10. Schematics of flow patterns mean gauge pressure p distributions (cross-sectional mean) for different boundary conditions based on momentum conservation considerations, assuming no viscous losses: (a)—closed top and bottom, (b)—open top, (c)—open bottom, (d)—open top and bottom. The pressure in (d) is equal to the outside pressure.

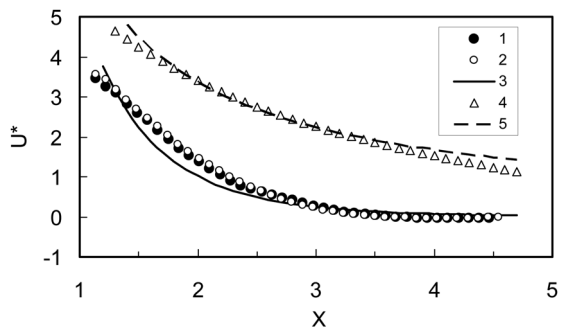

FIG. 12. Decay of dimensionless axial velocity $U^* = u^* D/J^{1/2}$ with distance $X = x/D$ for three experiments at $Re = 10\,100$: (1)—top open and bottom closed, (2)—bottom open and top closed, (3)—equation (16) for both top and bottom closed, (4)—both top and bottom open, (5)—Schlichting's solution for a free turbulent jet.

For the case of Fig. 10(d) no such opposing pressure gradients are possible, and hence the flow resistance is merely due to wall friction. Now the flow is free to preserve a significant amount of its momentum and stream through the cylinder (Fig. 11(c)).

The decay of mean maximum axial velocity u^* with axial distance x for three experiments with the same $Re = 10\,100$ but different boundary conditions is shown in Fig. 12. Dimensionless velocity $U^* = u^* D/J^{1/2}$ and distance $X = x/D$ are used in this graph (see Sec. III C). The data for the two cases (1 and 2 in Fig. 12) where one end is closed are practically undistinguishable. Empirical parameterization (solid line 3) derived below for the case where both the top and the bottom are closed satisfactorily describes the data of 1 and 2. The case 4 of Fig. 12, where both ends are opened, demonstrates different behavior. This flow belongs to the class of Craya-Gurtet flows,[18] and Schlichting's solution[16] for free turbulent jet (dashed line 5) satisfactorily describes its limiting behavior (Fig. 11(c)).

Based on above observations, we conclude that the case of jet issuing into a cylinder with both ends closed is generally similar to the case where only one end is closed. Using the mean velocity data shown in Fig. 11, streamlines in the (x-y) plane could be plotted, and an example is shown in Fig. 13. The mean flow therein is approximately axisymmetric and evinces large toroidal recirculation cells, as was schematized in Fig. 6(a).

Before proceeding further, we present a scaling analysis and discuss some predictions.

C. Scaling analysis

Consider jet-induced flow in a long cylinder of diameter D and length L ($\gg D$), wherein at least one end is closed (Fig. 2). The jet is emanating from a round nozzle of diameter d ($\ll D$), with a volume flux q. The kinematic viscosity and density of the fluid are ν and ρ respectively. The important governing dimensional parameters for the fully established flow are q, d, D, L, ν ρ and hence any flow characteristics A_i can be represented as

$$A_i = \Phi_i(q, d, D, L, \nu, \rho, x, y), \tag{2}$$

where x is the axial distance, y is the characteristic across flow distance, and Φ_i are unknown functions.

Experiments show that for $L \gg D$ the length of the cylinder is not important, given the mean motion stops at a finite distance $x^* < L$. Also, for $d \ll D$, the volume flux q and nozzle diameter d are important only in a combined form,

$$J = q^2/s, \quad s = \pi d^2/4, \tag{3}$$

which is the jet momentum flux (jet intensity). Following the standard approach[15,16,19] we use the *kinematic* momentum flux (momentum flux per unit mass), because for incompressible homogeneous fluids the fluid density does not play a role in flow dynamics, except for determining the pressure as in Eq. (1).

In dimensionless form J is equal to the jet Reynolds number (e.g., Batchelor[15])

$$Re = J^{1/2}/\nu \tag{4}$$

when the flow is turbulent ($Re \gg 1$), the molecular viscosity is assumed unimportant in the spirit of the Reynolds number similarity, whence (2) can be reduced to five dimensional governing parameters

$$A_i = \Phi_i(D, J, \rho, x, y), \tag{5}$$

three of which have independent dimensions. Thus, in dimensionless form only two independent parameters remain (cf., Barenblatt[20]). Choosing the characteristic length l and time τ scales

$$l = D, \quad \tau = D^2/J^{1/2}, \tag{6}$$

the velocity scale is

$$l/\tau = J^{1/2}/D, \tag{7}$$

the turbulent (effective) viscosity

$$l^2/\tau = J^{1/2} \tag{8}$$

and pressure

$$(l/\tau)^2 \rho = J\rho/D^2, \tag{9}$$

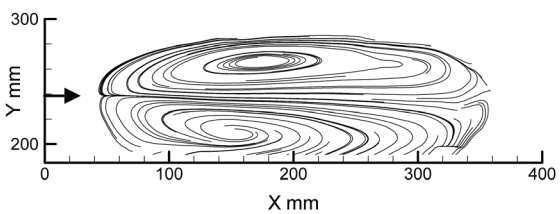

FIG. 13. Selected mean streamlines for Fig. 11(a) (x-y plane). The mean flow is approximately axisymmetric and streamlines show the cross-section of toroidal recirculation cells of Fig. 6(a). Arrow shows the nozzle.

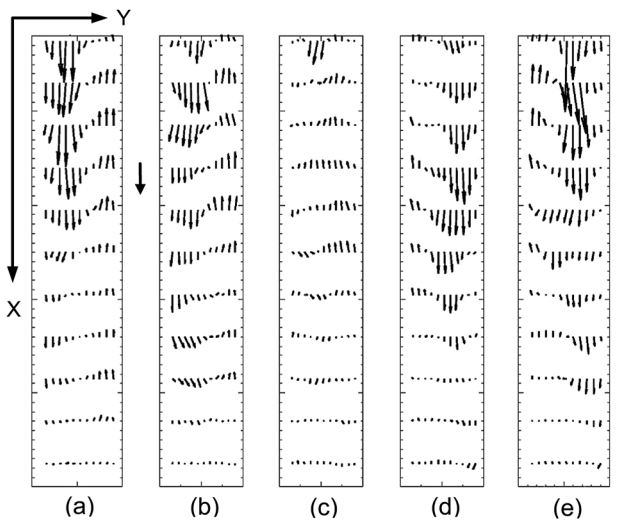

FIG. 14. Instantaneous velocity (black arrows) maps for different times at $Re = 10\,100$: $t = 0$ (a), 1.3 (b), 2.6 (c), 3.9 (d), 5.2 s (e). The plots span half of the period of oscillations ($1/f \approx 10.4$ s). The velocity scale (10 cm s^{-1}) is shown by solid vertical arrow between (a) and (b).

where Eq. (9) is consistent with Eq. (1). Using these scales and Eq. (5), certain predictions are possible.

For example, the mean dimensionless axial velocity $\overline{U} = \frac{\overline{u}}{J^{1/2}/D}$ becomes

$$\overline{U} = \overline{U}(X, Y), \tag{10}$$

where $\overline{U}(X, Y)$ is a function of the dimensionless coordinates $X = x/D, \quad Y = y/D$. Similarly, the dimensionless critical distance X^* and flow oscillation frequency F becomes

$$X^* = x^*/D = C, \quad F = \frac{f}{J^{1/2}/D^2} = C^*, \tag{11}$$

where C and C^* are constants (X and Y are unimportant for X^* and F). Note that F can be interpreted as the Strouhal number, which is expected to be a constant for an inertially dominated flow. These predictions can be verified via measurements.

It is reiterated that the above predictions are valid only for narrow ($L/D \gg 1$) cylinders where L can be neglected and self similarity is viable. For $L/D \sim 1$, no complete similarity is expected, given the appearance of an additional length scale L and this case is beyond the scope of this paper. Similarly, when $d \ll D$ (in our case $d/D \approx 1/60$), the nozzle can be considered as a "point" source of momentum flux J (Schlichting,[16] Batchelor[15]), thus permitting exclusion of nozzle diameter from the analysis.

For two-dimensional flows, similar considerations yield the following:

$$l = D, \quad \tau = D^{3/2}/I^{1/2}, \tag{12}$$

where I is the jet momentum flux per unit jet width, whence the predictions equivalent to (11) become

$$X^* = x^*/D = C_{2D}, \quad F = \frac{f}{I^{1/2}/D^{3/2}} = C^*_{2D}. \tag{13}$$

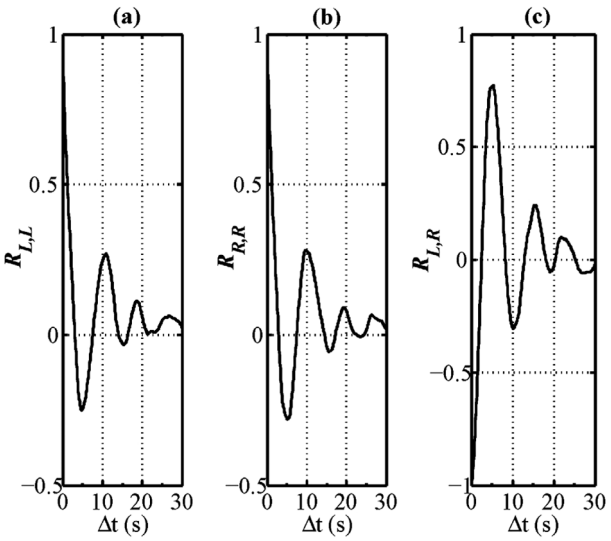

FIG. 15. Time autocorrelations averaged over x. (a)—R_{LL} at $y = -0.25D$, (b)—R_{RR} at $y = 0.25D$, (c)—cross-correlation R_{LR} (between $y = -0.25D$ and $y = 0.25D$). $Re = 10\,100$. The time correlations show $1/f \approx 10.4$ s.

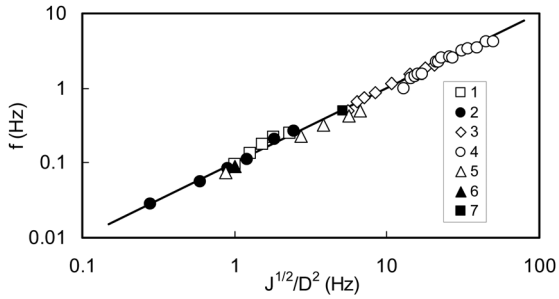

FIG. 16. Frequency of oscillations f versus frequency scale $J^{1/2}/D^2$. Symbols—experimental data, solid line—Eq. (11) with $C^* = 0.1$. Data from: (1)—present experiments, $d/D = 0.016$ (PIV); (2)—present experiments, $d/D = 0.016$ (DVC); (3)—Ref. 2 ($\beta = 0.2$), (4)—Ref. 2 ($\beta = 0.3$), (5)—Ref. 10 ($\beta = 1$), (6)—present experiments, $d/D = 0.016$ (angular momentum); (7)—present experiment, $d/D = 0.037$ (DVC).

In general, the coefficients C_{2D}, C^*_{2D} may differ from C, C^* in Eq. (11).

IV. BASIC FLOW CHARACTERISTICS

A. Frequency of flow oscillations

Quantitative data on f were obtained using DVC recordings and PIV data. First, relatively long (100-200 s) DVC recordings with frequency 10 Hz were made for each run. Then these recordings were replayed several times at a slow speed (1-5 Hz) and the mean (over the recording period) values of f were obtained for each run. The scatter of the data for each run did not exceed ±10%. Thereafter, by using PIV data, instantaneous velocity profiles were plotted (e.g., Fig. 14) and the mean f for each data set was obtained.

In addition, using the same PIV data, the time correlation function $R_{uu}(x, y, \Delta t)$

$$R_{uu}(x, y, \Delta t) = \frac{\langle u(x, y, t)u(x, y, t + \Delta t)\rangle}{\langle u^2(x, y, t)\rangle} \tag{14}$$

for the axial velocity u at $y = \pm 0.25D$ was calculated ($\langle \ldots. \rangle$ is the time averaging) for $1 < x/D < 3$ and averaged over x. Typical time autocorrelations $R_{LL}(y,\Delta t)$ at $y = -0.25D$ (near the left side) and $R_{RR}(y,\Delta t)$ at $y = 0.25D$ (near the right side) as well as time cross-correlations $R_{LR}(y,\Delta t)$ (between

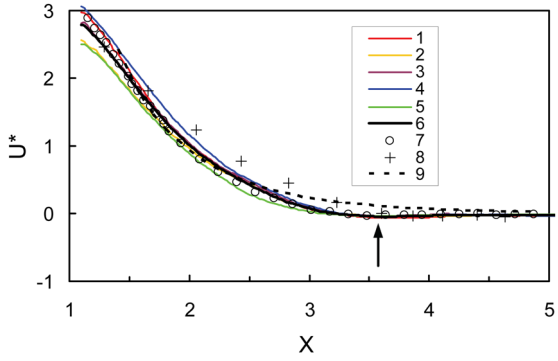

FIG. 17. (Color online) Decay of mean dimensionless axial velocity U^* with dimensionless distance X are shown by colour lines (1-5) for $d/D = 0.016$ at $Re = 10\,100$ (1), 12 700 (2), 15 300 (3), 17 900 (4), 23 100 (5); (6)—mean over all experiments with larger cylinder, (7)—smaller cylinder, $d/D = 0.037$, (8)—data from Ref. 7, $Re = 150\,000$, $d/D = 0.195$, (9)—Eq. (16).

$y = -0.25D$ and $y = 0.25D$) are shown in Fig. 15. The mean period $1/f$ of flow oscillations for each run was obtained by calculating the time shift Δt when the first maximum (for autocorrelation) or minimum (for cross-correlations) was observed.

The results of different methods are summarized in Fig. 16, where f (in Hz) is plotted as a function of the frequency scale (6), $1/\tau = J^{1/2}/D^2$ for experiments with different jet intensities J. The agreement with Eq. (11) is clear, and the best fit gives $C^* = 0.1$ with regression coefficient $R^2 = 0.96$.

To our knowledge, no previous frequency data are available for 3D geometries, but some exist for 2D and are included in Fig. 16 with appropriate adjustments. To make direct comparisons with the 3D data, Eq. (13) can be written as

$$F = \frac{f}{(J/H)^{1/2}/D^{3/2}} = \frac{f\beta^{1/2}}{J^{1/2}/D^2} = C^*_{2D}, \qquad (15)$$

where $J = IH$ is the net momentum flux, $\beta = H/D$ the aspect ratio, and H is the width of the 2D jet.

Using f and Re in Ref. 2 ($\beta = 0.2$, 0.3, $Re = 1000$-3600) and Ref. 10 ($\beta = 1$, $Re = 500$-4000), the modified frequencies $f\beta^{1/2}$ were calculated and are shown in Fig. 16, which fall on our best fit (solid) line, indicating that coefficients in Eqs. (11) and (15) are the same for both geometries. The fact that 2D experiments conducted using air jets give similar results to those of water jets strongly supports similarity scaling of Sec. III C.

B. Mean flow characteristics

The mean dimensionless centreline axial velocity $U^*(X) = \overline{U}(X, Y = 0)$ as a function of dimensionless distance X is shown in Fig. 17 by the colored lines (1-5) for all runs conducted with larger cylinder, $d/D = 0.016$. The mean of all is shown by solid line (6), which illustrates approximate independence of Reynolds number. The data for smaller cylinder $d/D = 0.037$ are shown by open circles.

For comparison, data from previous work are also shown in Fig. 17 by crosses (8). These were taken from Ref. 7, where visually a similar dimensionless velocity distribution could be found for $Re = 150\,000$ and $d/D = 0.195$. Nevertheless, there is one important difference; in Ref. 7, the cylinder diameter D and the nozzle exit velocity u_0 are used as length and velocity scales (hence invoking d as an independent variable). We proposed the same length scale D but a different velocity scale $J^{1/2}/D$, where the jet momentum flux J is used as the sole parameter describing the jet, a composite of u_0 and d. In comparing our data with those of Ref. 7, we have used $J^{1/2}/D$, and a satisfactory agreement was noted over a range of d/D (0.016-0.195) and Re (10 000-150 000), as shown in Fig. 17.

As can be seen, U^* smoothly decreases with X, crosses zero at $X \approx 3.2$ and shows (see black arrow) a small but measurable negative value until $X \approx 3.6$ before becoming vanishingly small, yielding a critical distance $X^* \approx 3.6$ and $C \approx 3.6$ for Eq. (11). The exact value of C is not very important, as it depends on the definition of X^*. More importantly,

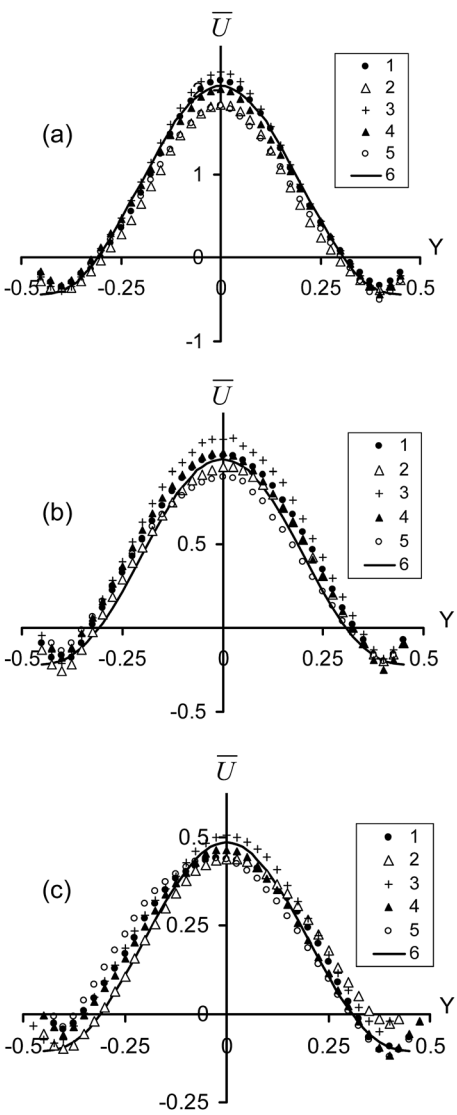

FIG. 18. Transverse profiles of dimensionless mean axial velocity $\overline{U}(Y)$ for different dimensionless axial distances: $X = 1.5$ (a), 2 (b), 2.5 (c) and for $Re = 10\,100$ (1), 12 700 (2), 15 300 (3), 17 900 (4), 23 100 (5). Solid line (6) is Eq. (17).

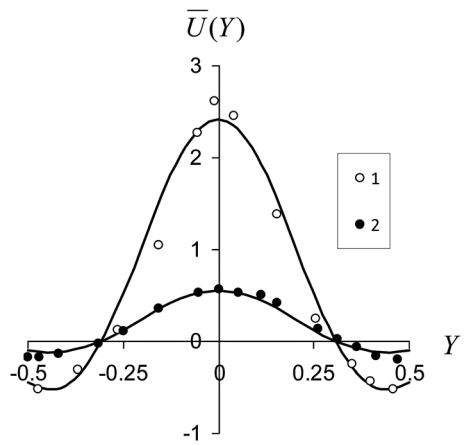

FIG. 19. Transverse profiles of dimensionless mean axial velocity $\overline{U}(Y)$ for $X = 1.3$ (1), 2.7 (2). Symbols—experimental data from Ref. 7 for $Re = 150\,000$, $d/D = 0.195$, solid line is Eq. (17).

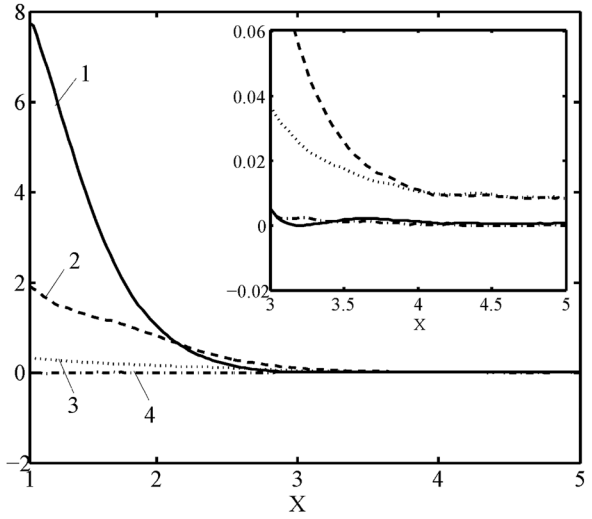

FIG. 20. The maximum values of squared dimensionless mean axial velocity U^{*2} and turbulence statistics of U' and V' versus X: (1)—U^{*2}, (2)—$\langle U'^2\rangle$, (3)—$\langle V'^2\rangle$, (4)—$\langle U'V'\rangle$. Averaged values over all experiments conducted at different Reynolds numbers are shown.

X^* remains approximately the same for different experimental conditions (Fig. 17), thus supporting our similarity arguments.

Empirically, the mean centreline axial velocity can be approximately fitted to the function

$$U^*(X) = \frac{A}{X\exp(X)}, \tag{16}$$

which is shown in Fig. 17 by the dashed line (9), with the constant $A = 13.8$. Note that Eq. (16) takes into account that, at small X, U^* ought to decay inversely with X, as in a free jet. But at larger X it is expected to decay exponentially.[7,11,12]

To parameterize $\overline{U}(X,Y)$, it is possible to propose $\overline{U}(X,Y) = U^*(X) \times \overline{U}(Y)$ with $\overline{U}(Y) = \sin(BY)/BY$, which gives

$$\overline{U}(X,Y) = \frac{A}{X\exp(X)} \times \frac{\sin(BY)}{BY}, \tag{17}$$

where $B = const$. Figure 18 shows Eq. (17) with $A = 13.8$ and $B = 10.2$ by solid lines. In the near-wall thin boundary layer the measurement accuracy is modest, and thus the velocity amplitude of reverse flow is most probably underestimated. For comparison, available data (Ref. 7) for transverse dimensionless mean axial velocity profiles are shown in Fig. 19, and Eq. (17) describes these data very well.

Although Eq. (17) does not capture no-slip condition at a finite radial distance, it correctly describes the mean axial velocity profiles over a broad range of parameters, Re (10 000-150 000) and d/D (0.016-0.195), and employs a minimal number of empirical coefficients. It is expected to be a valuable formula in engineering applications.

C. Basic turbulent flow characteristics

Although turbulent flow characteristics in similar geometries have been measured previously,[11,12] the main interest has been on flow characteristics at larger distances $X > X^*$, in the area of weak "diffusive" turbulence with negligible mean velocity. To complement, here we present turbulence data at smaller distances, where the mean flow is present. The second order moments for U' and V' are shown in Fig. 20 as a function of X. The data for different Reynolds numbers satisfactorily collapsed (within $\pm 10\%$), and for clarity the average over all Reynolds numbers are shown. The mean values of U^{*2} are also shown for comparison. For U^* we used averaged data given by solid line (6) in Fig. 17. In Fig. 20, at smaller distances ($X < 2$), only $\langle U'^2\rangle$ is significant and it is comparable to U^{*2} while $\langle V'^2\rangle$ is smaller by a factor of 5. At larger distances both U^{*2} and $\langle U'^2\rangle$ decay in similar ways and are comparable. Beyond $X \approx 3.6$ all flow characteristics become very small. The cross-correlations $\langle U'V'\rangle$ are negligibly small at all distances. Inset in Fig. 20 is an enlarged view of flow characteristics at $X > 3$.

V. CONCLUSIONS

The evolution of a turbulent jet released into a low aspect ratio (width/height) cylinder under neutrally stratified conditions was investigated experimentally using PIV and digital imaging methods. The study was focused on: (i) observations of general flow structure and instabilities that lead to periodic oscillations intrinsic to jets; (ii) the roles of (top/bottom) boundary conditions and resulting pressure adjustments that cause jet to disintegrate into diffusive turbulence, and (iii) the parameterization of flow velocities and jet oscillating frequency. Using scaling arguments and the assumption of Reynolds number similarity, the governing dimensional parameters were reduced to two: the jet intensity J (kinematic momentum flux) and container width D, which leads to characteristic length D and time $D^2/J^{1/2}$ scales. The scaling for the critical distance for jet disintegration and the frequency of flow oscillations was proposed and experimentally confirmed. The characteristics of rotational instability were addressed using angular momentum of the flow.

Based on experiments with different top/bottom conditions it was argued that the principle results of our study, conducted using a jet issuing into a cylinder with both ends closed, should be valid to geometries with one end closed. For the former case, empirical parameterization was proposed for mean velocity distribution.

Using the scaling laws developed, useful estimates for flow quantities in the SPR caverns could be obtained.

TABLE I. Comparison of laboratory and SPR field parameters.

	L (cm)	D (cm)	q (cm^3/s)	d (cm)	J (cm^4/s^2)	ν (cm^2/s)	Re	x^* (cm)	f (Hz)	$J^{1/2}/D$ (Cm/s)
SPR	7×10^4	7000	3×10^5	25	1.8×10^8	0.1	1.3×10^5	25 000	2.5×10^{-5}	2
Lab	65	10	8-40	0.165	$(1\text{-}65) \times 10^3$	0.01	$(3\text{-}25) \times 10^3$	36	0.03-0.27	3-25

Typical parameters for laboratory experiments and SPR cavern are given in Table I (1/*f* being the period of oscillations). Using Eq. (11) with $C = 3.6$ and $C^* = 0.1$, the dimensional values of x^* and f for SPR caverns were calculated and are shown in Table I.

In SPR caverns, however, the crude oil is slightly stably (density) stratified with typical buoyancy frequencies in the range $N \approx 10^{-3}$-10^{-4} s^{-1}. Vertical jet mixing in such cases can be characterized by the jet-cavern Froude number

$$Fr = u^*/DN = \frac{J^{1/2}}{D^2 N} U^*(X) = Fr_0 U^*(X), \qquad (18)$$

where u^* is the typical vertical velocity and $U^*(X)$ is given in Eq. (16). For $Fr \geq 1$, mixing may be significant, while it is insignificant for $Fr \ll 1$. Using $Fr_0 = J^{1/2}/D^2 N \approx 0.3$-3 as typical for SPR caverns, one arrives at the conclusion that an oil column of dimensionless depth X^* is subjected to significant vertical velocities and prone to be well mixed. Also, in a low aspect ratio cavern, the flow is expected to oscillate with a period 1/*f*, which is half a day. Such flow vacillations may induce additional mixing considering SPR degas periods are ~3 months. To investigate the effects of stratification, additional work was conducted and the results will be presented in a separate communication.

ACKNOWLEDGMENTS

This work was supported by the Sandia National Laboratories, which is operated by Lockheed Martin Corporation for the United States Department of Energy's National Nuclear Security Administration under Contract No. DE-AC04-94AL85000.

[1]D. L. Lord and D. K. Rudeen, "Summary of Degas II performance at the US strategic petroleum reserve big hill site," Technical Report No. SAND2007-5564, 53 p., Sandia National Laboratories, Albuquerque, NM (2007).
[2]E. Villermaux and E. J. Hopfinger, "Self-sustained oscillations of a confined jet: a case study for the non-linear delayed saturation model," Physica D **72**, 230 (1994).
[3]B. M. Gebert, M. R. Davidson, and M. J. Rudman, "Computed oscillations of a confined submerged liquid jet," Appl. Math. Model. **22**, 843 (1998).
[4]D. M. Denisikhina, A. Bassina, D. A. Nikulin, and M. K. Strelets, "Numerical simulation of self-excited oscillation of a turbulent jet flowing into a rectangular cavity," High Temp. **43**(4), 568 (2005).
[5]N. A. Molloy and P. L. Taylor, "Oscillatory flow of a jet into a blind cavity," Nature (London) **224**, 1192 (1969).
[6]B. C. Khoo, T. C. Chew, P. S. Heng, and H. K. Kong, "Turbulence characterization of a confined jet using PIV," Exp. Fluids **13**, 350 (1992).
[7]F. Risso and J. Fabre, "Diffusive turbulence in a confined jet experiment," J. Fluid Mech. **337**, 233 (1997).
[8]N. J. Lawson, "Self-sustained oscillation of a submerged jet in a thin rectangular cavity," J. Fluids Struct. **15**, 59 (2001).
[9]H. Liu, S. H. Winoto, A. Dilip, and D. A. Shah, "Velocity measurements within confined turbulent jets: application to cardiovalvular regurgitation," Ann. Biomed. Eng. **25**, 939 (1997).
[10]A. Mataouia and R. Schiestelb, "Unsteady phenomena of an oscillating turbulent jet flow inside a cavity: effect of aspect ratio," J. Fluids Struct. **25**, 60 (2009).
[11]A. A. Sonin, M. A. Shimko, and J. H. Chun, "Vapor condensation onto a turbulent liquid - I. The steady condensation rate as a function of liquid-side turbulence," Int. J. Heat Mass Transfer, **29**(9), 1319 (1986).
[12]J. S. Brown, B. C. Khoo, and A. A. Sonin, "Rate correlation for condensation of pure vapor on turbulent, subcooled liquid," Int. J. Heat Mass Transfer **33**(9), 2001 (1990).
[13]M. Merzkirch, *Flow Visualization* (Academic Press, New York, 1974).
[14]G. J. Nathan, S. J. Hill, and R. E. Luxton, "An axisymmetric 'fluidic' nozzle to generate jet precession," J. Fluid. Mech. **370**, 347 (1998).
[15]G. K. Batchelor, *Introduction to Fluid Mechanic* (Cambridge University Press, Cambridge, 1970).
[16]H. Schlichting, *Boundary Layer Theory* (McGraw-Hill, New York, 1979).
[17]B. J. Cantwell, "Viscous starting jets," J. Fluid Mech. **173**, 159 (1986).
[18]A. Revuelta, C. Martinez-Bazan, A. L. Sanchez, and A. Linan, "Laminar craya-curtet jets," Phys. Fluids **16**(1), 208 (2004).
[19]P. A. Davidson, *Turbulence: An Introduction for Scientist and Engineers* (Cambridge University Press, Cambridge, 2004).
[20]G. I. Barenblatt, *Scaling, Self-similarity, and Intermediate Asymptotics* (Cambridge University Press, Cambridge, 1996).